Covalency Competition in the Quadruple Perovskite CdCu_3Fe_4O_12

Covalency Competition in the Quadruple Perovskite $CdCu_3Fe_4O_{12}$

Ikuya Yamada,[a,b] Akihiko Takamatsu,[a] Naoaki Hayashi,[c] Hidekazu Ikeno*[a,d]*

[a]*Nanoscience and Nanotechnology Research Center, Osaka Prefecture University, 1-2 Gakuen-cho, Naka-ku, Sakai, Osaka 599-8570, Japan*

[b]*Department of Materials Science, Graduate School of Engineering, Osaka Prefecture University, 1-2 Gakuen-cho, Naka-ku, Sakai, Osaka 599-8570, Japan*

[c]*Research Institute for Production Development, 15 Shimogamo-morimoto-cho, Sakyo-ku, Kyoto 606-0805, Japan*

[d]*Precursory Research for Embryonic Science and Technology (PRESTO), Japan Science and Technology Agency (JST), 4-1-8 Honcho Kawaguchi, Saitama 332-0012, Japan*

ABSTRACT

Cadmium ions (Cd^{2+}) are similar to calcium ions (Ca^{2+}) in size, whereas the Cd^{2+} tend to form covalent bonds with the neighboring anions because of the high electronegativity. The covalent Cd–O bonds affect other metal-oxygen bonds, inducing drastic changes in crystal structures and electronic states. Herein, we demonstrate high-pressure synthesis, crystal structure, and properties of a new quadruple perovskite $CdCu_3Fe_4O_{12}$. This compound exhibits an electronic phase transition accompanying a charge disproportionation of Fe ions without charge ordering below ~200 K, unlike charge-disproportionation transition with rock-salt-type charge ordering for $CaCu_3Fe_4O_{12}$. First-principle calculations and Mössbauer spectroscopy display that covalent Cd–O bonds effectively suppress the Fe–O bond covalency, resulting in the electronic state different from that of $CaCu_3Fe_4O_{12}$. This finding proposes covalency competition among constituent metal ions dominating electronic states of complex metal oxides.

1. INTRODUCTION

Chemical bonding is of fundamental interest in solid-state compounds.[1-4] Intrinsic properties of solids such as hardness, electrical conductivity, and thermal stability are strongly dependent on covalency between constituent atoms. Thus, in-depth understanding of covalency (or ionicity) is essential to elucidate structure-property relationships in solids. Chemical bonding of transition metal oxides has been widely investigated because of a great variety of their constituent elements, structures, and properties. The perovskite oxides ABO_3 have three-dimensional networks of *B*–O bonds, whose characters are adjustable by ionic sizes of *A*- and *B*-site ions, thus being considered as a promising system for fundamental investigations and prospective applications.[5-7] The *B*-sites for perovskite structure are usually occupied by smaller transition metal ions in the d-block, whereas the *A*-sites are occupied by larger cations in the s-block (e.g. Na^+, Ca^{2+}) and rare-earth (e.g. Y^{3+}, La^{3+}) metal cations. On the other hand, several elements in the p- and d-blocks (e.g. Ag^+, Pb^{2+}, Bi^{3+}) can occupy *A*-sites, and their relatively high electronegativities induce substantial changes in properties. For instance, stereochemical effects of Pb^{2+}/Bi^{3+} ions cause lattice distortions, leading to ferroelectricity,[8,9] and covalent Ag–O bonds serve to achieve high hole-mobility.[10] The Cd^{2+} ions are almost isometric to the Ca^{2+} ions ($r_{Cd^{2+}}$ = 1.31 Å; $r_{Ca^{2+}}$ = 1.34 Å in twelvefold coordination)[11,12] while their Pauling electronegativities (χ) are quite different (χ_{Cd} = 1.69; χ_{Ca} = 1.00). The effects of different bonding characters between Ca–O and Cd–O bonds on properties were investigated in $ATiO_3$ (*A* = Ca, Cd) perovskites.[13,14] $CaTiO_3$ crystallizes in the orthorhombic $GdFeO_3$-type perovskite structure at room temperature and retains its symmetry down to the lowest temperature. Despite of the isomorphism at room temperature, $CdTiO_3$ undergoes a ferroelectric phase transition below 85 K, which is interpreted as effects of strong covalency of Cd–O bonds on particular phonon

modes.[13,15,16] Further explorations for intriguing phenomena induced by Cd–O covalency have not been found probably because of the limited number of Cd-containing perovskites reported.[17,18] Therefore, it is unclear how the formation of Cd–O covalent bonds affects the properties of *B*–O bonds in other systems.

The quadruple perovskite series, $AA'_3B_4O_{12}$, is a derivative of the simple ABO_3 perovskite. Three quarters of original *A*-sites (= *A'*-sites) are occupied by small transition metal ions (Cu^{2+}, Mn^{3+}, Fe^{2+}, Co^{2+}, Pd^{2+}, etc.) in pseudosquare coordination whereas the remaining fourth (= *A*-sites) are occupied by typical larger ions (Na^+, Ca^{2+}, La^{3+}, etc.) in icosahedral coordination.[19-23] It was recently reported that the *A*-sites also tolerate a wide range of ions such as Mn^{2+} and Cu^+,[24-26] in addition to smaller rare-earth metal ions (Y^{3+}, Lu^{3+}, etc.).[27] The Cd ions are also incorporated into *A*-sites in the quadruple perovskites such as $CdCu_3Ti_4O_{12}$,[28,29] $CdCu_3Ru_4O_{12}$,[30] $CdCu_3Mn_4O_{12}$,[31] and $CdMn_7O_{12}$.[32] In any compounds, the covalency of Cd–O bonds does not seem to drastically change their properties because of insensitivity of electronic states to bonding properties. On the other hand, it was recently reported that the quadruple perovskites with unusual valence Fe ions (typically Fe^{4+}), $ACu_3Fe_4O_{12}$ (A = Ca^{2+}, Sr^{2+}, trivalent rare-earth metals R^{3+}, Bi^{3+}, and Ce^{4+}), demonstrate a wide range of intriguing properties strongly depending on the valences and/or sizes of *A*-site ions: charge disproportionation ($2Fe^{4+} \rightarrow Fe^{3+} + Fe^{5+}$), charge ordering/disordering of the Fe^{3+} and Fe^{5+} ions, bidirectional intersite charge transfers ($Cu^{2+} + Fe^{4+} \rightleftarrows Cu^{3+} + Fe^{3+}$), negative thermal expansion, and high catalytic activity for oxygen evolution reaction.[33-42] Their electronic states are sensitive to the character of Fe–O bonds. There is a common correlation between Fe–O bond length and ^{57}Fe Mössbauer isomer shift (*IS*) in $Ca_{1-x}Sr_xCu_3Fe_4O_{12}$ and $RCu_3Fe_4O_{12}$ (R = trivalent rare-earth metals).[43] The Fe–O bond covalency is flexibly controlled by the Fe–O bond elongation and can be reasonably

estimated by *IS* values. The *IS* value of ~0.17 mm s^{-1} is a boundary of two distinct low-temperature electronic phases: (1) charge-disproportionated/ordered phase (*IS* < ~0.17 mm s^{-1}) and (2) Cu-to-Fe electron-charge-transferred and/or charge-disproportionated/disordered phase (*IS* > ~0.17 mm s^{-1}). The interatomic distances are typical factors determining covalency in transition metal compounds.[44] whereas Ca substitution by more electronegative Cd affects bond covalency and possibly induces a drastic change in electronic states.

In this article, we demonstrate structural and electronic properties of $CdCu_3Fe_4O_{12}$, which was synthesized under ultra-high-pressure and high-temperature of 20 GPa and 1000 ºC. Structural and spectroscopic data revealed that the low-temperature electronic phase transformation in $CdCu_3Fe_4O_{12}$ substantially differs from that in $CaCu_3Fe_4O_{12}$. Covalency competition between Cd–O and Fe–O bonds reasonably explain the differences in structures and properties between $CdCu_3Fe_4O_{12}$ and $CaCu_3Fe_4O_{12}$. This finding proposes that competition in covalent bond formation among constituent metal ions dominate electronic properties of solids.

2. EXPERIMENTAL

A precursor was obtained using the polymerized complex method.[37,45] A mixture of $Cd(NO_3)_2 \cdot 4H_2O$ (99.9%), $Cu(NO_3)_2 \cdot 3H_2O$ (99.9%), and $Fe(NO_3)_3 \cdot 9H_2O$ (99.9%) at a molar ratio of 1:3:4 was dissolved in nitric acid solution (ca. 5 M), to which a five-fold excess of citric acid and a one-fold excess of 1,2-ethanediol were added while stirring. The resulting solution was heated to 573 K, while stirring, and maintained at this temperature for 1 h to dry. Subsequently, the dried powder was fired using a furnace at 673 K for 1 h and 948 K for 12 h in air with occasional grindings. The afforded precursor was mixed with an oxidizing agent $KClO_4$ (99.9%) in a mass ratio of 7:1. The sample mixture was sealed off during the treatment in a platinum

capsule. The capsule was placed into a (Mg,Co)O pressure medium and compressed to pressures up to 20 GPa using a high-pressure apparatus. The sample was subsequently heated to 1273 K in 20 min, maintained at this temperature for 30 min, and quenched to room temperature. During the heat treatment, the applied pressure was maintained. The pressure was slowly released after the heat treatment. The obtained polycrystalline sample was washed several times with distilled water.

Synchrotron X-ray powder diffraction (SXRD) experiments were performed at the BL02B2 beamline of SPring-8 using samples contained in Lindemann glass capillary tubes with an inner diameter of 0.2 mm. The wavelength used was determined to be 0.42043 Å using a CeO_2 standard. Structure parameters were refined by Rietveld analysis using the program RIETAN-FP.[46] The crystal structures were drawn using the VESTA software.[47] The soft X-ray absorption spectrum (XAS) of Cu L_3-edge was collected at 300 K using the total electron yield method at the BL27SU beamline of SPring-8. The energy resolution was greater than 5000. The X-ray absorption near-edge structure (XANES) spectra of Cu K-edge for $CdCu_3Fe_4O_{12}$ were collected at 10 and 300 K at the BL14B1 beamline of SPring-8. The ^{57}Fe Mössbauer spectroscopy measurement was performed in transmission geometry using ^{57}Co/Rh as a radiation source and α-Fe as a control for the velocity calibration and isomer shift. The collected Mössbauer spectra were fitted computationally using the Lorentzian function. Magnetization measurements were conducted using a superconducting quantum interference device (SQUID, Quantum Design MPMS-XL) between 5 and 300 K under external magnetic fields between 0.1 and 50 kOe. Since no well-sintered sample was obtained, the electric resistivity was not investigated in this study.

Density functional theory (DFT) calculations of $CaCu_3Fe_4O_{12}$ and $CdCu_3Fe_4O_{12}$ were performed using the projector augmented-wave method as implemented in VASP code.[48] The exchange-correlation interaction was treated within the framework of the generalized gradient approximation (GGA) with Perdew-Burke-Ernzerhof (PBE) functional.[49] The on-site Coulomb interactions on the localized 3d electrons were treated with the GGA+U approach[50] with $U_{eff} = 7$ and 4 eV for Cu and Fe, respectively, for both $CaCu_3Fe_4O_{12}$ and $CdCu_3Fe_4O_{12}$. The U values were taken from the literature,[51] in which the electronic structure of $CaCu_3Fe_4O_{12}$ was investigated using DFT. The PAW data set with radial cutoffs 2.3 Å for Ca, Cd, Cu and Fe and 1.52 Å for O, where Ca-3s, 4s, 3p Cd-5s, 4d, Cu-3d, 4s, Fe-3d, 4s and O-2s, 2p were described as valence electrons. The plane-wave cutoff energy was set to 500 eV. A 6×6×6 k-point sampling following the Monkhorst-Pack scheme was used.[52] The lattice constants and internal coordinates were optimized until the total energy difference and residual forces converge to less than 10^{-5} and 10^{-2} eV/Å, respectively. Space groups of $CaCu_3Fe_4O_{12}$ and $CdCu_3Fe_4O_{12}$ are considered as $Im\bar{3}$ to compare charge distribution at room temperature. $CaCu_3Fe_4O_{12}$ is reported to be ferrimagnet, in which magnetic moments of Fe are ordered in the same direction and moments of Cu are opposite to them.[33,53] Thus, the electronic structure of $CaCu_3Fe_4O_{12}$ was calculated for the ferrimagnetic phase. The magnetic structure of $CdCu_3Fe_4O_{12}$ was not able to be determined precisely by experiment. In the present work, DFT calculations of $CdCu_3Fe_4O_{12}$ were made with three different magnetic structures: i) the ferrimagnetic phase, ii) the ferromagnetic phase in which all magnetic moments of Fe and Cu are ordered ferromagnetically, and iii) the G-type antiferromagnetic phase in which Fe magnetic moments are arranged in the G-type antiferromagnetic order while Cu ions have no magnetic moment. We found that the ferrimagnetic phase was most stable among them. The calculated energy differences of the

ferromagnetic and G-type antiferromagnetic phases when the ferrimagnetic phase is used as a reference were 0.49 and 0.11 eV per formula unit, respectively. Therefore, the ferrimagnetic structure was adopted for $CdCu_3Fe_4O_{12}$ in this study.

3. RESULTS

Crystal Structure

The samples obtained at pressures below 20 GPa contained much amount of impurity phases. In contrast, the sample synthesized at 20 GPa included insignificant amount of impurity phases. We adopted the sample obtained at 20 GPa in this study. Figure 1 displays the observed SXRD patterns of $CdCu_3Fe_4O_{12}$ at 100 and 300 K and Rietveld refinement results. The primary phase at 300 K could be indexed in the cubic quadruple perovskite (space group: $Im\bar{3}$, No. 204) with a lattice constant a of ~7.30 Å. There were small amounts of impurity phases: α-Fe_2O_3 (~3 wt%) and CuO (~4 wt%). Since $CdCu_3Fe_4O_{12}$ exhibited no anomaly in temperature evolution of a-axis length, the crystal structures at all temperatures were refined using the same structure model as the RT phase. After the final refinements, we obtained satisfactory reliability factors: R_{wp} (~2%) and R_B (1.5–2%) at all temperatures. The structure parameters obtained from the refinement at 100 and 300 K are listed in Table 1. The a-axis length of $CdCu_3Fe_4O_{12}$ (7.299 Å) at 300 K is almost identical to that of $CaCu_3Fe_4O_{12}$ (7.294 Å).[42] The Cu−O and Fe−O bond lengths are also identical for $CdCu_3Fe_4O_{12}$ and $CaCu_3Fe_4O_{12}$ at this temperature. However, the Cd−O bond (~2.60 Å) was slightly longer than the Ca–O bond (~2.58 Å). This implies different bonding characters between them. The bond valence sums (BVSs) were calculated from the refinement results (Table 1). The BVS of Ca was +2.27,[42] slightly larger than the value expected from divalency (+2), indicating that the Ca^{2+} ions are overbonded by the 12 neighboring oxide ions. In

contrast, BVS of Cd was 1.82, slightly smaller than +2, exhibiting underbonding of Cd–O bonds for $CdCu_3Fe_4O_{12}$, as reported in $CdMn_7O_{12}$.[32]

The temperature dependence of Cu–O and Fe–O bond lengths displayed clear difference between $CdCu_3Fe_4O_{12}$ and $CaCu_3Fe_4O_{12}$ (Figure 2). The Cu–O bonds expanded and average Fe–O bond lengths decreased below 210 K for $CaCu_3Fe_4O_{12}$, which is attributed to the Fe-to-Cu electron charge transfer ($3Cu^{\sim 2.4+} + 4Fe^{\sim 3.65+} \rightarrow 3Cu^{\sim 2.2+} + 4Fe^{\sim 3.8+}$), as reported previously.[42] In contrast, the Cu−O bonds shrank (~0.1 Å) and Fe–O bonds expanded very slightly below 200 K for $CdCu_3Fe_4O_{12}$. This indicates the opposite type of charge transfer (Cu-to-Fe electron charge transfer), compared to $CaCu_3Fe_4O_{12}$. This type of charge transfer is predominant for $SrCu_3Fe_4O_{12}$, not $CaCu_3Fe_4O_{12}$.[40]

Valence States

Valence states of $CdCu_3Fe_4O_{12}$ were investigated by X-ray absorption and Mössbauer spectroscopies. Figure 3a shows the Cu L_3-edge XAS at 300 K. The spectrum contained a shoulder ~932 eV, in addition to the main peak at ~930 eV. This ensures the mixed valence state of Cu ions (i.e. $Cu^{(2+\delta)+}$) for $CdCu_3Fe_4O_{12}$ as in $CaCu_3Fe_4O_{12}$ and $SrCu_3Fe_4O_{12}$.[40,42] Figure 3b illustrates the Cu K-edge XANES spectra at 10 and 300 K for $CdCu_3Fe_4O_{12}$. The edge position at 300 K was almost identical to those of $CaCu_3Fe_4O_{12}$ and $SrCu_3Fe_4O_{12}$ (Figure S1 in the Supporting Information), estimating the Cu valence as ~2.4. The Cu K-edge shifted to higher energy side on cooling down to 10 K, indicating the Cu oxidation by Cu-to-Fe electron charge transfer, as in $SrCu_3Fe_4O_{12}$. The magnitude of Cu oxidation was estimated to be ~0.13 valence unit (v.u.) from the edge shift of ~0.25 eV, in accordance to the reference data. Thus, the charge transfer process in $CdCu_3Fe_4O_{12}$ is represented as $3Cu^{\sim 2.4+} + 4Fe^{\sim 3.65+} \rightarrow 3Cu^{\sim 2.5+} + 4Fe^{\sim 3.55+}$.

The ^{57}Fe Mössbauer spectra at temperatures between 4 and 300 K are illustrated in Figure 4 and the obtained hyperfine parameters are listed in Table 2. The spectrum at 300 K consisted of a paramagnetic singlet (*B*-site Fe, 94 atom%) and a doublet (*A'*-site Fe, 3 atom%) from $CdCu_3Fe_4O_{12}$, and a sextet (3 atom%) from the α-Fe_2O_3 impurity. The primary singlet component had an intermediate *IS* value (0.176 mm s^{-1}) between $CaCu_3Fe_4O_{12}$ (0.16 mm s^{-1}) and $SrCu_3Fe_4O_{12}$ (0.20 mm s^{-1}).[40,42] The spectrum split into multiple magnetic sextet components below 200 K: one Fe^{5+} (29 atom%) and three Fe^{3+} (69 atom% in total). The spectrum at 4 K is more similar to that of the solid solution $Ca_{0.6}Sr_{0.4}Cu_3Fe_4O_{12}$ [one Fe^{5+} (31 atom%) and three Fe^{3+} (69 atom% in total)] rather than those of $CaCu_3Fe_4O_{12}$ [one Fe^{5+} (39 atom%) and two Fe^{3+} (61 atom% in total)] and $SrCu_3Fe_4O_{12}$ [one Fe^{5+} (18 atom%) and one Fe^{3+} (82 atom%)].[40,42,43] This observation ensures that the low-temperature electronic state of $CdCu_3Fe_4O_{12}$ is distinguished from that of $CaCu_3Fe_4O_{12}$.

Magnetic Property

Figure 5a displays temperature dependence of the magnetic susceptibility for $CdCu_3Fe_4O_{12}$. A clear magnetic transition at ~190 K was observed but the behavior below this temperature was not simple. This is interpreted as coexistence of ferromagnetic (Curie temperature ~190 K) and antiferromagnetic (Néel temperature ~170 K) domains. It is noted that this behavior is very similar to the magnetic susceptibility of $Ca_{0.6}Sr_{0.4}Cu_3Fe_4O_{12}$,[43] in which ferromagnetic charge-ordered and antiferromagnetic charge-disordered phases coexist. The isothermal magnetization curve of $CdCu_3Fe_4O_{12}$ at 5 K was also similar to that of $Ca_{0.6}Sr_{0.4}Cu_3Fe_4O_{12}$ (Figure 5b). The magnetization value of $CdCu_3Fe_4O_{12}$ at 50 kOe was much smaller than the ferromagnetic saturation magnetization (~10 μ_B per formula unit) of $CaCu_3Fe_4O_{12}$ and rather close to that of $Ca_{0.6}Sr_{0.4}Cu_3Fe_4O_{12}$ (~3 μ_B per formula unit). These

features confirm that the low-temperature magnetic phase of $CdCu_3Fe_4O_{12}$ is different from the ferrimagnetic phase of $CaCu_3Fe_4O_{12}$.

4. DISCUSSION

The above-demonstrated experimental data reveal that $CdCu_3Fe_4O_{12}$ undergoes a charge disproportionation and a Cu-to-Fe electron charge transfer below 200 K as follows: $3Cu^{\sim 2.4+} + 4Fe^{\sim 3.65+} \rightarrow 3Cu^{\sim 2.5+} + 4Fe^{\sim 3.55+}$; $Fe^{\sim 3.55+} \rightarrow \sim 0.3Fe^{5+} + \sim 0.7Fe^{3+}$. This feature is similar to that of $Ca_{0.6}Sr_{0.4}Cu_3Fe_4O_{12}$ and well distinguished from $CaCu_3Fe_4O_{12}$. $Ca_{0.6}Sr_{0.4}Cu_3Fe_4O_{12}$ accommodates an intermediate Fe–O bonding character between ionic ($SrCu_3Fe_4O_{12}$) and covalent ($CaCu_3Fe_4O_{12}$) Fe–O bonds, which can be controlled by weight-averaged ionic size of *A*-site ions. The Fe–O bonding character of $CdCu_3Fe_4O_{12}$ was evaluated in the *IS* versus Fe−O bond length diagram, according to a previous study.[43] Figure 6 shows the *IS* as a function of Fe–O bond length at 300 K. It is noted that the data point of $CdCu_3Fe_4O_{12}$ is substantially deviated from $CaCu_3Fe_4O_{12}$–$SrCu_3Fe_4O_{12}$ solid solution line, where the Fe–O bond covalency is primarily dependent on the Fe–O bond length. In other words, the Fe–O bonds of $CdCu_3Fe_4O_{12}$ have more ionic character despite of almost the same Fe–O bond lengths as $CaCu_3Fe_4O_{12}$. In this diagram, the electronic phases are divided at *IS*~0.17 mm s^{-1} for $ACu_3Fe_4O_{12}$ system (*A* = Ca/Sr, R^{3+}).[43] $CdCu_3Fe_4O_{12}$ has an *IS* value similar to that of $Ca_{0.6}Sr_{0.4}Cu_3Fe_4O_{12}$, indicating near covalent character. The intermediate Fe–O bonding character for $CdCu_3Fe_4O_{12}$ is not apparently expected because similar Fe–O bond lengths to $CaCu_3Fe_4O_{12}$. To elucidate the difference between Cd–O and Ca–O bonds, we compared electronic states of $CdCu_3Fe_4O_{12}$ and $CaCu_3Fe_4O_{12}$ obtained from DFT calculations.

Figure 7a displays density of states (DOS) of $CdCu_3Fe_4O_{12}$ and $CaCu_3Fe_4O_{12}$ obtained from DFT calculations. It is obvious that the valence bands for both compounds mainly consist of Cu, Fe, and O orbitals. In contrast, the Ca and Cd orbitals less contribute to the valence band. To examine their contribution in detail, the partial DOS of Ca-s, p and Cd-s, p, d orbitals are displayed in Figure 7b. The d orbital DOS of Cd ion is almost fully occupied in a range of –7 and 0 eV, which overlaps the valence band. The s and p (mainly 5s and 5p) orbitals of Cd ion are partially occupied below the Fermi level, although these orbitals are expected to be empty in a simple ionic model with $[Kr]4d^{10}$ electron configuration. This indicates that 5s and 5p orbitals of Cd ion are well hybridized with O 2p orbitals because of strong covalent character of Cd–O bond, as shown in Tl–O bond for $TlMnO_3$.[54] In contrast, no substantial DOSs of s, p-orbitals were observed in the valence band of $CaCu_3Fe_4O_{12}$, indicating less covalency between Ca and O ions.

Figure 7c shows electron density distributions of $CdCu_3Fe_4O_{12}$ and $CaCu_3Fe_4O_{12}$ obtained from DFT calculations. Substantial electron density exists between Cu and O ions for both oxides, confirming strong covalency of Cu–O bonds, as demonstrated experimentally in a previous work.[41] Little electron density is observed between Ca and O atoms as expected from strong ionic character of Ca–O bond. In contrast, remarkable electron density is confirmed between Cd and O atoms. This is well explained by orbital hybridization of Cd 5s, 5p orbitals with O 2p orbital, as shown in the DOS calculations. Thus, we conclude that the Cd ions form more covalent bonds with O ions, simultaneously weakening the covalency Fe–O bonds because of covalency competition.

CONCLUSION

In summary, a new quadruple perovskite oxide $CdCu_3Fe_4O_{12}$ was synthesized under ultra-high pressure of 20 GPa and its structural and electronic properties were investigated. The low-temperature charge-disproportionated electronic phase was different between nominally isoelectronic compounds, $CdCu_3Fe_4O_{12}$ and $CaCu_3Fe_4O_{12}$. Theoretical calculation and experimental spectroscopy study demonstrate that the covalent Cd–O bond suppresses the of Fe–O bond covalency. This derives clear differences in low-temperature electronic transformations. This finding proposes that competition of bond covalency play a crucial role in electronic properties of transition metal oxides.

ASSOCIATED CONTENT

Supporting Information.

Cu K-edge XANES spectra of $ACu_3Fe_4O_{12}$ (A = Cd, Ca, and Sr) (PDF)

AUTHOR INFORMATION

Corresponding Author

*E-mail: yamada@mtr.osakafu-u.ac.jp (I.Y.); h-ikeno@21c.osakafu-u.ac.jp (H.I.)

Notes

The authors declare no competing financial interest.

ACKNOWLEDGMENT

The authors thank Hidenobu Etani and Shohei Marukawa for the support of sample preparation. The synchrotron radiation experiments were performed at SPring-8 with the approval of JASRI (Proposal Numbers 2015B1879, 2016A1044, and 2017A1209). This work was supported by

JSPS KAKENHI (Grant Numbers 16H04220, 16H00893, and 26106518) and Toray Science Foundation.

REFERENCES

(1) Harrison, W. A. *Electronic Structure and the Properties of Solids*; Dover Publications: New York, 1989.
(2) Cox, P. A. *Transition Metal Oxides: An Introduction to Their Structure and Properties*; Oxford University Press: Oxford, 2010.
(3) Burdett, J. K. *Chemical Bonding in Solids*; Oxford University Press: Oxford, 1995.
(4) Brown, I. D. *The Chemical Bond in Inorganic Chemistry: The Bond Valence Model*; Oxford University Press: Oxford, 2001.
(5) Mitchell, R. H. *Perovskites: Modern and Ancient*; Almaz Press: Thunder Bay, 2002.
(6) Granger, P.; VParvulescu, V. I.; Kaliaguine, S.; W., P. *Perovskites and Related Mixed Oxides: Concepts and Applications*; Wiley-VCH: Weinheim, Germany, 2016.
(7) Tilley, R. J. D. *Perovskites: Structure-Property Relationships*; John Wiley & Sons: New York, 2016.
(8) Kuroiwa, Y.; Aoyagi, S.; Sawada, A.; Harada, J.; Nishibori, E.; Takata, M.; Sakata, M. Evidence for Pb-O covalency in tetragonal $PbTiO_3$. *Phys. Rev. Lett.* **2001**, *87*, 2176011-2176014.
(9) Kimura, T.; Kawamoto, S.; Yamada, I.; Azuma, M.; Takano, M.; Tokura, Y. Magnetocapacitance effect in multiferroic $BiMnO_3$. *Phys. Rev. B* **2003**, *67*, 180401.
(10) Nazir, S.; Upadhyay Kahaly, M.; Schwingenschlögl, U. High mobility of the strongly confined hole gas in $AgTaO_3/SrTiO_3$. *Appl. Phys. Lett.* **2012**, *100*, 201607.
(11) Shannon, R. D. Revised Effective Ionic-Radii and Systematic Studies of Interatomic Distances in Halides and Chalcogenides. *Acta Crystallogr., Sect. A: Found. Adv.* **1976**, *32*, 751-767.
(12) Cohen, R. E. Origin of Ferroelectricity in Perovskite Oxides. *Nature* **1992**, *358*, 136-138.
(13) Taniguchi, H.; Soon, H. P.; Shimizu, T.; Moriwake, H.; Shan, Y. J.; Itoh, M. Mechanism for suppression of ferroelectricity in $Cd_{1-x}Ca_xTiO_3$. *Phys. Rev. B* **2011**, *84*, 174106.
(14) Kennedy, B. J.; Zhou, Q.; Avdeev, M. The ferroelectric phase of $CdTiO_3$: A powder neutron diffraction study. *J. Solid State Chem.* **2011**, *184*, 2987-2993.
(15) Taniguchi, H.; Shan, Y. J.; Mori, H.; Itoh, M. Critical soft-mode dynamics and unusual anticrossing in $CdTiO_3$ studied by Raman scattering. *Phys. Rev. B* **2007**, *76*, 212103.
(16) Shan, Y. J.; Mori, H.; Tezuka, K.; Imoto, H.; Itoh, M. Ferroelectric Phase Transition in $CdTiO_3$ Single Crystal. *Ferroelectrics* **2003**, *284*, 107-112.
(17) Belik, A. A.; Takayama-Muromachi, E. High-pressure synthesis, crystal structures, and characterization of $CdVO_{3-\delta}$ and solid solutions $CdVO_3$–$NaVO_3$. *J. Solid State Chem.* **2006**, *179*, 1650-1658.
(18) Shannon, R. D.; Gillson, J. L.; Bouchard, R. J. Single crystal synthesis and electrical properties of $CdSnO_3$, Cd_2SnO_4, In_2TeO_6 and $CdIn_2O_4$. *J. Phys. Chem. Solids* **1977**, *38*, 877-881.
(19) Chenavas, J.; Joubert, J. C.; Marezio, M.; Bochu, B. The synthesis and crystal structure of $CaCu_3Mn_4O_{12}$: A new ferromagnetic-perovskite-like compound. *J. Solid State Chem.* **1975**, *14*, 25-32.
(20) Bochu, B.; Chenavas, J.; Joubert, J. C.; Marezio, M. High pressure synthesis and crystal structure of a new series of perovskite-like compounds CMn_7O_{12} (C = Na, Ca, Cd, Sr, La, Nd). *J. Solid State Chem.* **1974**, *11*, 88-93.
(21) Leinenweber, K.; Linton, J.; Navrotsky, A.; Fei, Y.; Parise, J. B. High-pressure perovskites on the join $CaTiO_3$-$FeTiO_3$. *Phys. Chem. Miner.* **1995**, *22*, 251-258.
(22) Ovsyannikov, S. V.; Zainulin, Y. G.; Kadyrova, N. I.; Tyutyunnik, A. P.; Semenova, A. S.; Kasinathan, D.; Tsirlin, A. A.; Miyajima, N.; Karkin, A. E. New Antiferromagnetic Perovskite $CaCo_3V_4O_{12}$ Prepared at High-Pressure and High-Temperature Conditions. *Inorg. Chem.* **2013**, *52*, 11703-11710.
(23) Shiro, K.; Yamada, I.; Ikeda, N.; Ohgushi, K.; Mizumaki, M.; Takahashi, R.; Nishiyama, N.; Inoue, T.; Irifune, T. Pd^{2+}-Incorporated Perovskite $CaPd_3B_4O_{12}$ (B = Ti, V). *Inorg. Chem.* **2013**, *52*, 1604-1609.
(24) Akizuki, Y.; Yamada, I.; Fujita, K.; Nishiyama, N.; Irifune, T.; Yajima, T.; Kageyama, H.; Tanaka, K. A-site-ordered perovskite $MnCu_3V_4O_{12}$ with a 12-coordinated manganese(II). *Inorg. Chem.* **2013**, *52*, 11538-11543.

(25) Ovsyannikov, S. V.; Abakumov, A. M.; Tsirlin, A. A.; Schnelle, W.; Egoavil, R.; Verbeeck, J.; Van Tendeloo, G.; Glazyrin, K. V.; Hanfland, M.; Dubrovinsky, L. Perovskite-like Mn_2O_3: A Path to New Manganites. *Angew. Chem. Int. Ed.* **2013**, *52*, 1494-1498.
(26) Akizuki, Y.; Yamada, I.; Fujita, K.; Taga, K.; Kawakami, T.; Mizumaki, M.; Tanaka, K. Rattling in the Quadruple Perovskite $CuCu_3V_4O_{12}$. *Angew. Chem. Int. Ed.* **2015**, *54*, 10870-10874.
(27) Sanchez-Benitez, J.; Alonso, J. A.; Martinez-Lope, M. J.; de Andres, A.; Fernandez-Diaz, M. T. Enhancement of the Curie Temperature along the Perovskite Series $RCu_3Mn_4O_{12}$ Driven by Chemical Pressure of R^{3+} Cations (R = Rare Earths). *Inorg. Chem.* **2010**, *49*, 5679-5685.
(28) Homes, C. C.; Vogt, T.; Shapiro, S. M.; Wakimoto, S.; Subramanian, M. A.; Ramirez, A. P. Charge transfer in the high dielectric constant materials $CaCu_3Ti_4O_{12}$ and $CdCu_3Ti_4O_{12}$. *Phys. Rev. B* **2003**, *67*, 921061-921064.
(29) Sasaki, M.; Tashiro, T.; Abiko, K.; Kamimura, Y.; Takesada, M.; Onodera, A. Huge dielectric properties of $CdCu_3Ti_4O_{12}$ with CCTO structure. *Ferroelectrics* **2011**, *415*, 94-100.
(30) Labeau, M.; Bochu, B.; Joubert, J. C.; Chenavas, J. Synthèse et caractérisation cristallographique et physique d'une série de composés $ACu_3Ru_4O_{12}$ de type perovskite. *J. Solid State Chem.* **1980**, *33*, 257-261.
(31) Sánchez-Benítez, J.; Kayser, P.; Morales-García, A.; Martínez-Lope, M. J.; Mompeán, F. J.; Xu, J.; Jin, Z.; Alonso, J. A. Preparation, crystal structure, and magnetotransport properties of the new $CdCu_3Mn_4O_{12}$ Perovskite: A comparison with density functional theory calculations. *J. Phys. Chem. C* **2014**, *118*, 9652-9658.
(32) Glazkova, Y. S.; Terada, N.; Matsushita, Y.; Katsuya, Y.; Tanaka, M.; Sobolev, A. V.; Presniakov, I. A.; Belik, A. A. High-pressure synthesis, crystal structures, and properties of $CdMn_7O_{12}$ and $SrMn_7O_{12}$ perovskites. *Inorg. Chem.* **2015**, *54*, 9081-9091.
(33) Yamada, I.; Takata, K.; Hayashi, N.; Shinohara, S.; Azuma, M.; Mori, S.; Muranaka, S.; Shimakawa, Y.; Takano, M. A perovskite containing quadrivalent iron as a charge-disproportionated ferrimagnet. *Angew. Chem. Int. Ed.* **2008**, *47*, 7032-7035.
(34) Long, Y. W.; Hayashi, N.; Saito, T.; Azuma, M.; Muranaka, S.; Shimakawa, Y. Temperature-induced A-B intersite charge transfer in an A-site-ordered $LaCu_3Fe_4O_{12}$ perovskite. *Nature* **2009**, *458*, 60-63.
(35) Long, Y. W.; Saito, T.; Tohyama, T.; Oka, K.; Azuma, M.; Shimakawa, Y. Intermetallic Charge Transfer in A-Site-Ordered Double Perovskite $BiCu_3Fe_4O_{12}$. *Inorg. Chem.* **2009**, *48*, 8489-8492.
(36) Etani, H.; Yamada, I.; Ohgushi, K.; Hayashi, N.; Kusano, Y.; Mizumaki, M.; Kim, J.; Tsuji, N.; Takahashi, R.; Nishiyama, N.; Inoue, T.; Irifune, T.; Takano, M. Suppression of intersite charge transfer in charge-disproportionated perovskite $YCu_3Fe_4O_{12}$. *J. Am. Chem. Soc.* **2013**, *135*, 6100-6106.
(37) Yamada, I.; Tsuchida, K.; Ohgushi, K.; Hayashi, N.; Kim, J.; Tsuji, N.; Takahashi, R.; Matsushita, M.; Nishiyama, N.; Inoue, T.; Irifune, T.; Kato, K.; Takata, M.; Takano, M. Giant negative thermal expansion in the iron perovskite $SrCu_3Fe_4O_{12}$. *Angew. Chem. Int. Ed.* **2011**, *50*, 6579-6582.
(38) Yamada, I.; Shiro, K.; Oka, K.; Azuma, M.; Irifune, T. Direct observation of negative thermal expansion in $SrCu_3Fe_4O_{12}$. *J. Ceram. Soc. Jpn.* **2013**, *121*, 912-914.
(39) Yamada, I.; Etani, H.; Murakami, M.; Hayashi, N.; Kawakami, T.; Mizumaki, M.; Ueda, S.; Abe, H.; Liss, K. D.; Studer, A. J.; Ozaki, T.; Mori, S.; Takahashi, R.; Irifune, T. Charge-order melting in charge-disproportionated perovskite CeCu3Fe4O12. *Inorg. Chem.* **2014**, *53*, 11794-11801.
(40) Yamada, I.; Shiro, K.; Etani, H.; Marukawa, S.; Hayashi, N.; Mizumaki, M.; Kusano, Y.; Ueda, S.; Abe, H.; Irifune, T. Valence transitions in negative thermal expansion material $SrCu_3Fe_4O_{12}$. *Inorg. Chem.* **2014**, *53*, 10563-10569.
(41) Yagi, S.; Yamada, I.; Tsukasaki, H.; Seno, A.; Murakami, M.; Fujii, H.; Chen, H.; Umezawa, N.; Abe, H.; Nishiyama, N.; Mori, S. Covalency-reinforced oxygen evolution reaction catalyst. *Nat. Commun.* **2015**, *6*, 8249.
(42) Yamada, I.; Murakami, M.; Hayashi, N.; Mori, S. Inverse Charge Transfer in the Quadruple Perovskite $CaCu_3Fe_4O_{12}$. *Inorg. Chem.* **2016**, *55*, 1715-1719.
(43) Yamada, I.; Shiro, K.; Hayashi, N.; Kawaguchi, S.; Kawakami, T.; Takahashi, R.; Irifune, T. Structural and electronic transformations in quadruple iron perovskite $Ca_{1-x}Sr_xCu_3Fe_4O_{12}$. *J. Asian Ceram.*

Soc. **2017**, *5*, 169-175.
(44) Shannon, R. D.; Gumerman, P. S. Effect of covalence on interatomic distances in Cu^{+}, Ag^{+}, Tl^{+} and Pb^{2+} halides and chalcogenides. *J. Inorg. Nucl. Chem.* **1976**, *38*, 699-703.
(45) Kakihana, M. "Sol-Gel" preparation of high temperature superconducting oxides. *J. Sol-Gel Sci. Technol.* **1996**, *6*, 7-55.
(46) Izumi, F.; Momma, K. Three-Dimensional Visualization in Powder Diffraction. *Solid State Phenom.* **2007**, *130*, 15-20.
(47) Momma, K.; Izumi, F. VESTA 3 for three-dimensional visualization of crystal, volumetric and morphology data. *J. Appl. Crystallogr.* **2011**, *44*, 1272-1276.
(48) Blöchl, P. E. Projector augmented-wave method. *Phys. Rev. B* **1994**, *50*, 17953-17979.
(49) Perdew, J. P.; Burke, K.; Ernzerhof, M. Generalized Gradient Approximation Made Simple. *Phys. Rev. Lett.* **1996**, *77*, 3865-3868.
(50) Dudarev, S. L.; Botton, G. A.; Savrasov, S. Y.; Humphreys, C. J.; Sutton, A. P. Electron-energy-loss spectra and the structural stability of nickel oxide: An LSDA+U study. *Phys. Rev. B* **1998**, *57*, 1505-1509.
(51) Hao, X.; Xu, Y.; Gao, F.; Zhou, D.; Meng, J. Charge disproportionation in $CaCu_3Fe_4O_{12}$. *Phys. Rev. B* **2009**, *79*, 113101.
(52) Monkhorst, H. J.; Pack, J. D. Special points for Brillouin-zone integrations. *Phys. Rev. B* **1976**, *13*, 5188-5192.
(53) Mizumaki, M.; Chen, W. T.; Saito, T.; Yamada, I.; Attfield, J. P.; Shimakawa, Y. Direct observation of the ferrimagnetic coupling of A-site Cu and B-site Fe spins in charge-disproportionated $CaCu_3Fe_4O_{12}$. *Phys. Rev. B* **2011**, *84*, 094418.
(54) Yi, W.; Kumagai, Y.; Spaldin, N. A.; Matsushita, Y.; Sato, A.; Presniakov, I. A.; Sobolev, A. V.; Glazkova, Y. S.; Belik, A. A. Perovskite-Structure $TlMnO_3$: A New Manganite with New Properties. *Inorg. Chem.* **2014**, *53*, 9800-9808.
(55) Brown, I. D.; Altermatt, D. Bond-Valence Parameters Obtained From a Systematic Analysis of the Inorganic Crystal-Structure Database. *Acta Crystallogr., Sect. B: Struct. Sci., Cryst. Eng. Mater.* **1985**, *41*, 244-247.
(56) Woodward, P. M.; Cox, D. E.; Moshopoulou, E.; Sleight, A. W.; Morimoto, S. Structural studies of charge disproportionation and magnetic order in $CaFeO_3$. *Phys. Rev. B* **2000**, *62*, 844-855.

Table 1. Structure Parameters, Selected Bond Lengths, and BVS at 100 and 300 K for $CdCu_3Fe_4O_{12}$.[a]

Temperature (K)	100	300
Space group	$Im\bar{3}$	$Im\bar{3}$
a (Å)	7.29321(14)	7.29919(8)
x (O)	0.3105(3)	0.3091(3)
y (O)	0.1779(3)	0.1776(3)
U_{iso}(Cd)×1000 (Å^2)	2.4(3)	7.1(4)
U_{iso}(Cu)×1000 (Å^2)	4.4(2)	7.5(3)
U_{iso}(Fe)×1000 (Å^2)	0.88(19)	2.9(2)
U_{iso}(O)×1000 (Å^2)	5.8(5)	7.7(6)
Cd−O (×12) (Å)	2.610(2)	2.601(2)
Cu−O (×4) (Å)	1.8958(18)	1.9034(18)
Cu−O (×4) (Å)	2.726(3)	2.735(3)
Fe−O (×6) (Å)	1.9482(7)	1.9479(6)
Fe−O−Fe (deg.)	138.75(10)	139.02(10)
BVS(Cd) (v.u.)	1.78	1.82
BVS(Cu) (v.u.)	2.27	2.22
BVS(Fe) (v.u.)	3.73	3.72
R_{wp} (%)	2.181	2.182
R_B (%)	1.509	1.928
S	0.5622	0.5848

[a]Atomic sites: Cd 2*a* (0, 0, 0), Cu 6*b* (0, $^1/_2$, $^1/_2$), Fe 8*c* ($^1/_4$, $^1/_4$, $^1/_4$), O 24*g* (*x*, *y*, 0); The occupancy factor *g* for Cd, Cu, Fe, and O sites was fixed at unity. [b]The BVSs were calculated using the following parameters: $b_0 = 0.37$ for all atoms, $r_0 = 1.904$ for Cd, $r_0 = 1.649$ for Cu, and $r_0 = 1.772$ for Fe.[55,56]

Table 2. Hyperfine Parameters for $CdCu_3Fe_4O_{12}$ at 4 and 300 K Deduced from Mössbauer Spectra.[a]

Temperature (K)	Species	*IS* (mm s^{-1})	*HF* (kOe)	ΔE_q (mm s^{-1})	Abundance (%)
300	Fe (*B*-site)	0.176	0	0	94
	Fe (*A'*-site)	0.414	0	1.750	3
	Fe (α-Fe_2O_3)	0.373	515	−0.175	3
4	Fe^{5+}	0.075	226	0	29
	Fe^{3+}(1)	0.363	429	0	15
	Fe^{3+}(2)	0.410	465	0	13
	Fe^{3+}(3)	0.447	499	0	41
	Fe^{3+}(α-Fe_2O_3)	0.515	540	0.440	2

[a] *HF*: hyperfine field; ΔE_q: quadrupole splitting (doublet) or quadrupole shift (sextet). Quadrupole shifts were calculated as follows: $\Delta E_q = (S_2 – S_1)/2$, where S_1 is the deference between the position of first and second peak, and S_2 is the deference between the position of fifth and sixth peak in the sextet.

FIGURE CAPTIONS

Figure 1. Observed SXRD patterns of $CdCu_3Fe_4O_{12}$ at 100 and 300 K and the Rietveld refinement results. Dots (black) and solid lines (red) represent observed and calculated patterns, respectively. The difference between the observed and calculated patterns is shown at the bottom (blue). The vertical marks (green) indicate the Bragg reflection positions of $CdCu_3Fe_4O_{12}$ (upper), α-Fe_2O_3 (middle), and CuO (lower). The inset of upper panel shows the crystal structure of $ACu_3Fe_4O_{12}$.

Figure 2. Temperature dependence of the lattice constant *a* and selected bond lengths for $CdCu_3Fe_4O_{12}$ (red) and $CaCu_3Fe_4O_{12}$ (black). The filled circles for Fe−O bond lengths represent average values of $CaCu_3Fe_4O_{12}$. The data for $CaCu_3Fe_4O_{12}$ were taken from reference.[42]

Figure 3. X-ray absorption spectra of (a) Cu L_3-edge (300 K) and (a) Cu K-edge (10 and 300 K) for $CdCu_3Fe_4O_{12}$. The inset of (b) shows the enlarged spectra of the absorption edges.

Figure 4. Mössbauer spectra of $CdCu_3Fe_4O_{12}$ at temperatures between 4 and 300 K.

Figure 5. (a) Temperature dependence of the magnetic susceptibility and (b) isothermal magnetization for $CdCu_3Fe_4O_{12}$.

Figure 6. *IS* versus Fe–O bond length at ~300 K for $CdCu_3Fe_4O_{12}$ and $Ca_{1-x}Sr_xCu_3Fe_4O_{12}$. The red and blue circles represent the type of low-temperature phase, red: charge-disproportionated and charge-ordered phase, blue: charge-disproportionated and charge-disordered phase. The $Ca_{0.6}Sr_{0.4}Cu_3Fe_4O_{12}$ (red circle with blue border) locates around phase boundary. The data for $Ca_{1-x}Sr_xCu_3Fe_4O_{12}$ were taken from reference.[40,42,43]

Figure 7. (a) DOS of ACu$_3$Fe$_4$O$_{12}$ (A = Cd, Ca) and (b) Partial DOS of Cd and Ca ions. The values averaged between majority and minority spins are shown. The zero energy is set to the Fermi level. (c) Electron density distributions of ACu$_3$Fe$_4$O$_{12}$ (A = Cd, Ca). The equi-density level is 0.025 e/Bohr^3 (= 0.319 e/Å^3).

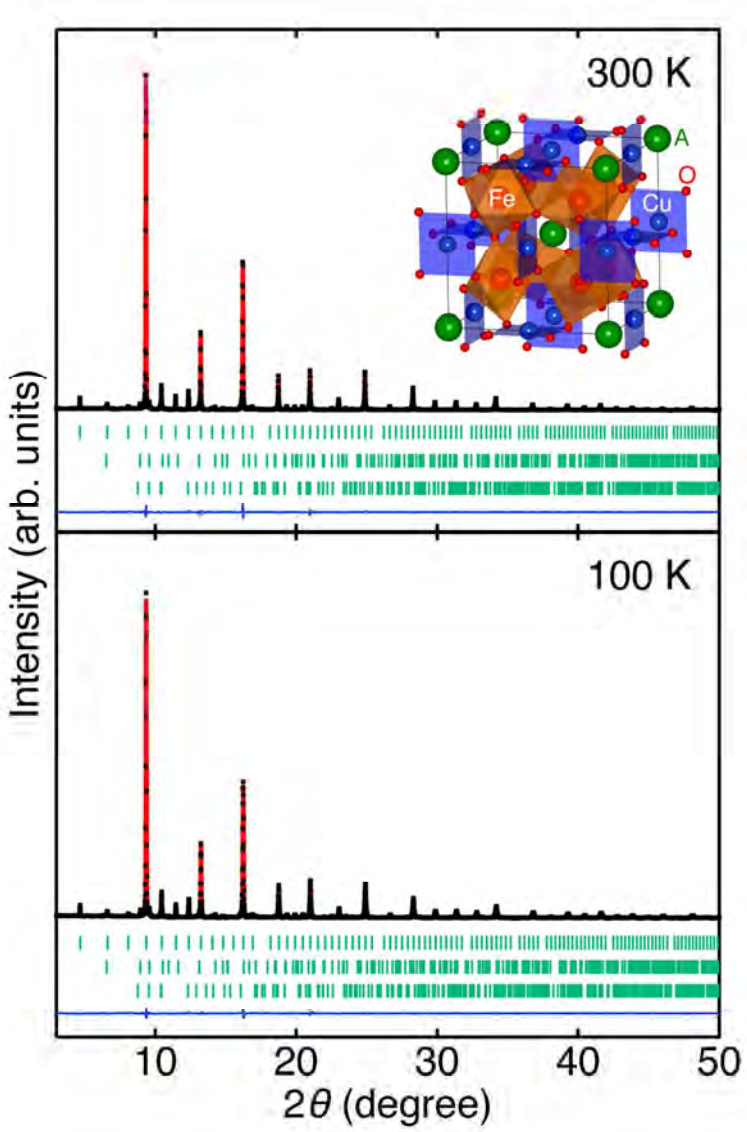

Figure 1

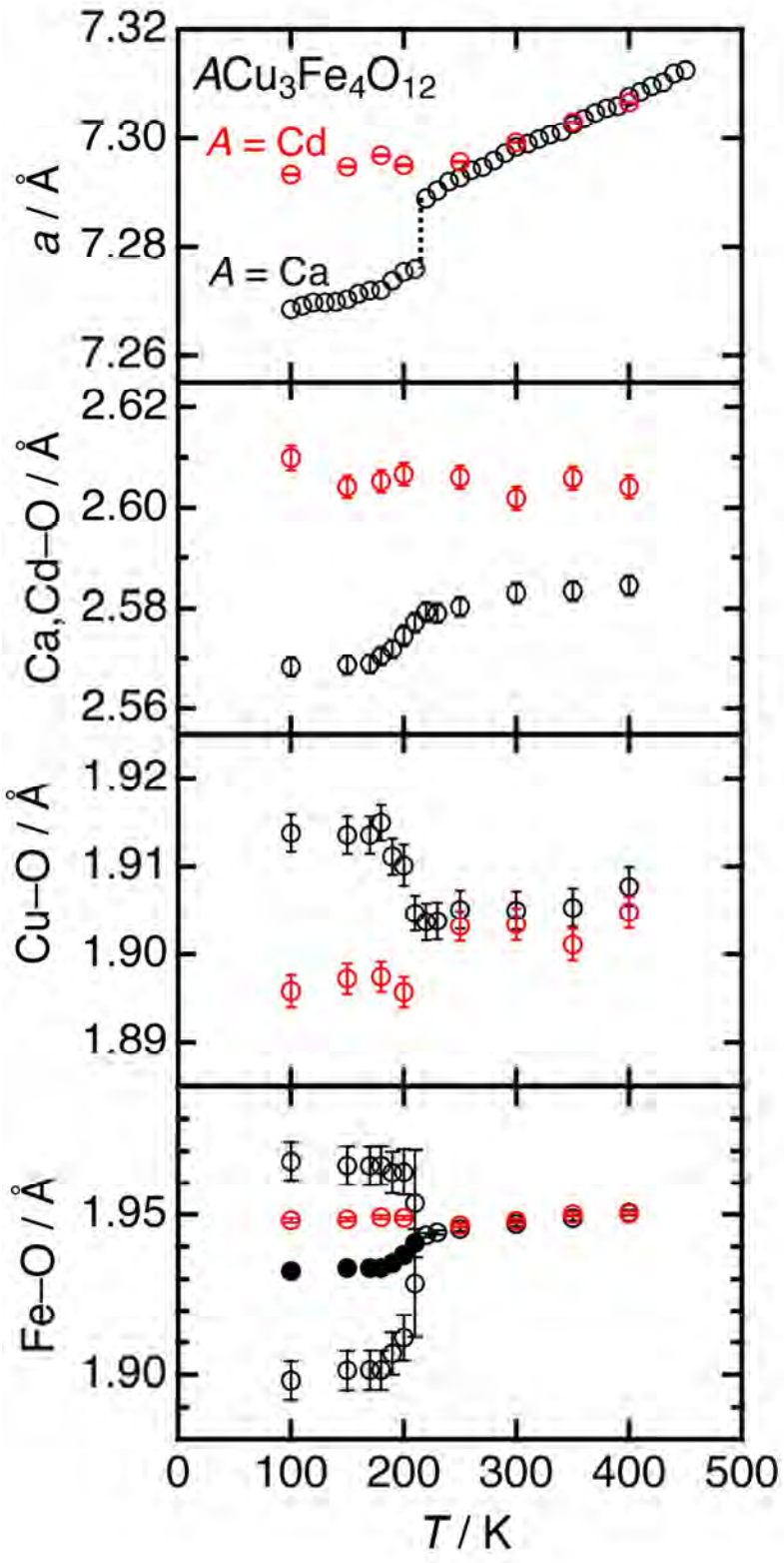
$ACu_3Fe_4O_{12}$
A = Cd
A = Ca
a / Å
Ca,Cd–O / Å
Cu–O / Å
Fe–O / Å
7.32
7.30
7.28
7.26
2.62
2.60
2.58
2.56
1.92
1.91
1.90
1.89
1.95
1.90
0
100
200
300
400
500
T / K

Figure 2

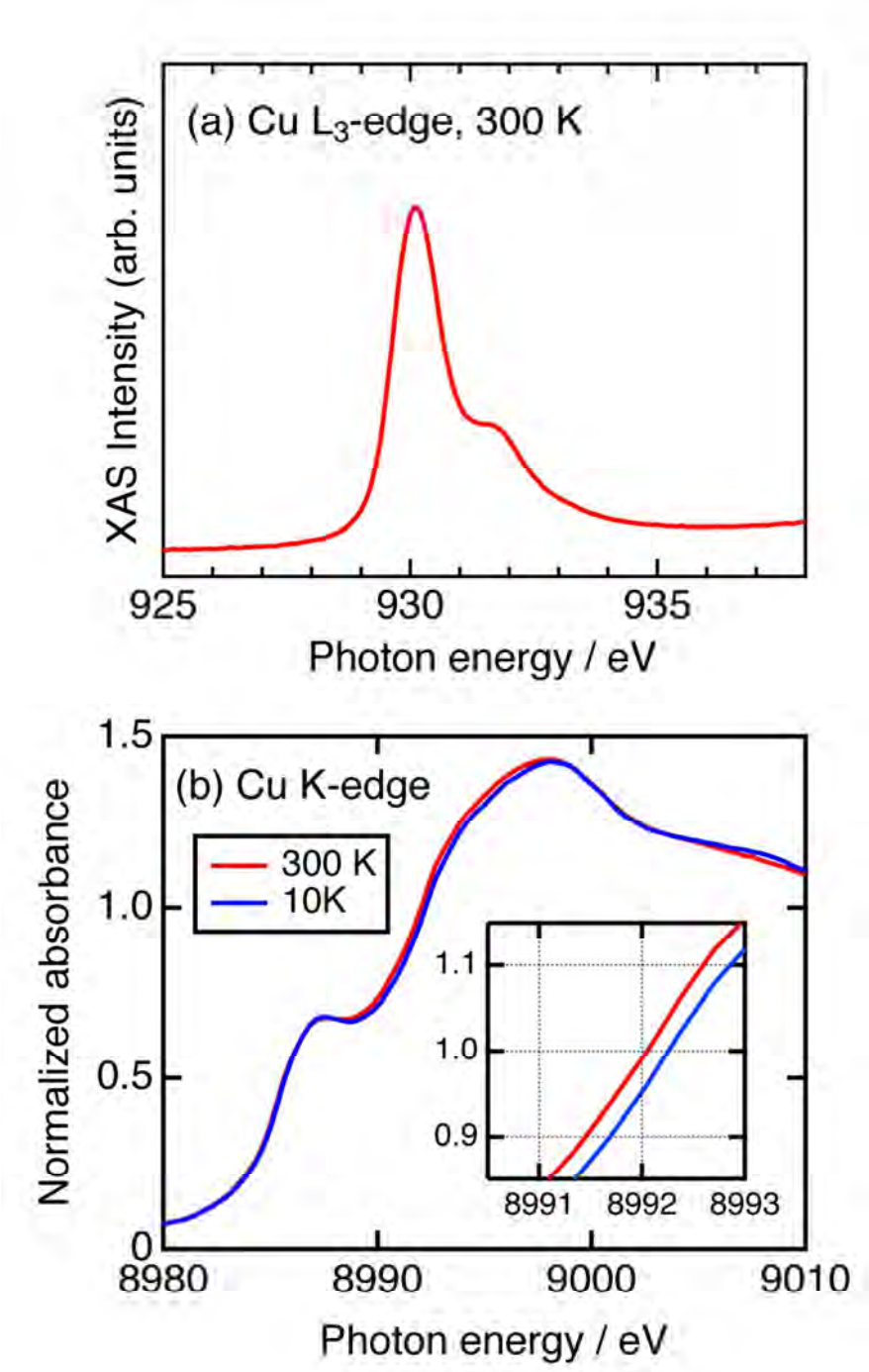
(a) Cu L3-edge, 300 K
XAS Intensity (arb. units)
925
930
935
Photon energy / eV
(b) Cu K-edge
300 K
10K
Normalized absorbance
1.5
1.0
0.5
0
1.1
1.0
0.9
8991
8992
8993
8980
8990
9000
9010
Photon energy / eV

Figure 3

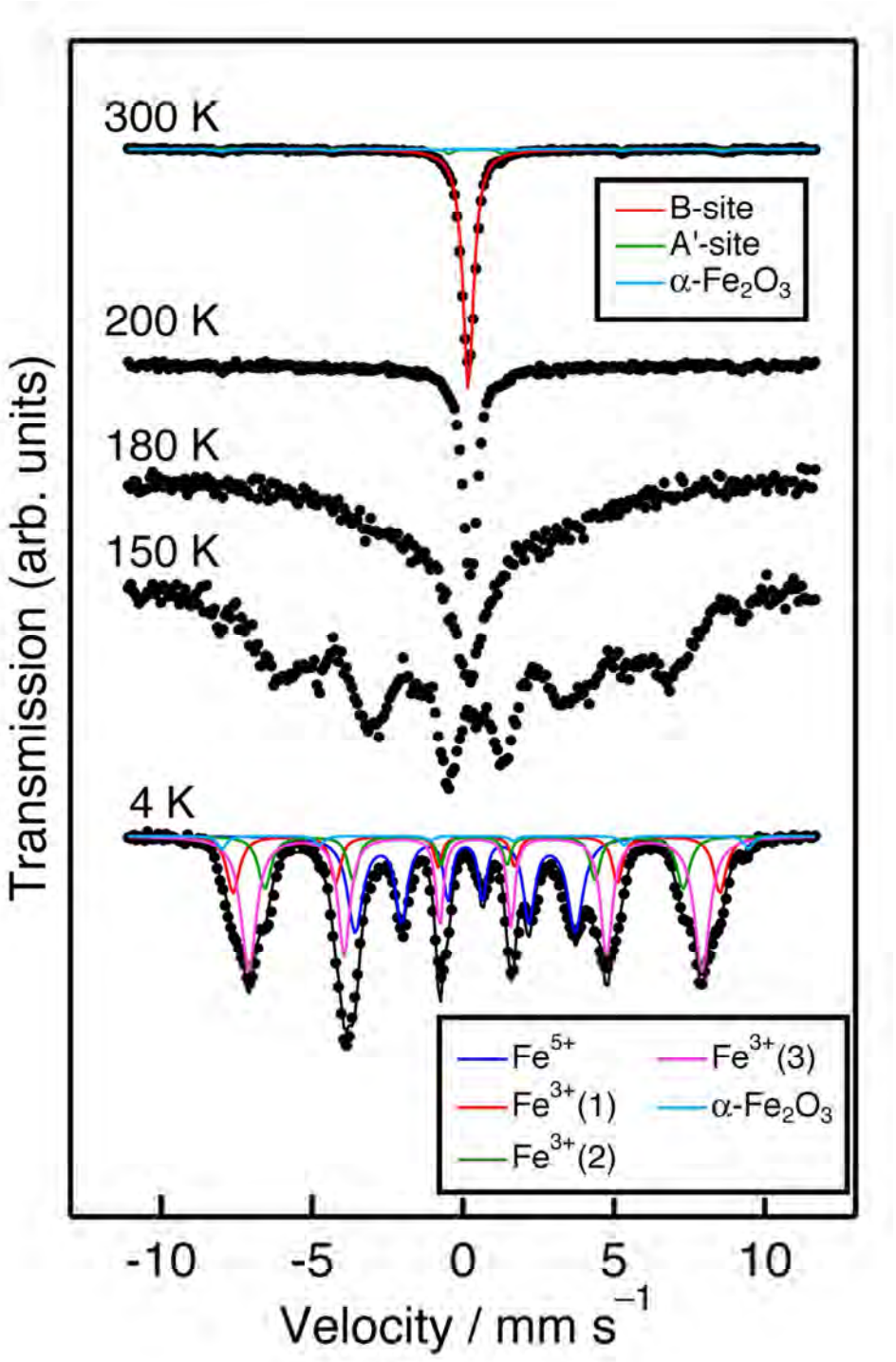
300 K
200 K
180 K
150 K
4 K
B-site
A'-site
α-Fe2O3
Fe5+
Fe3+(1)
Fe3+(2)
Fe3+(3)
α-Fe2O3
Transmission (arb. units)
-10
-5
0
5
10
Velocity / mm s−1

Figure 4

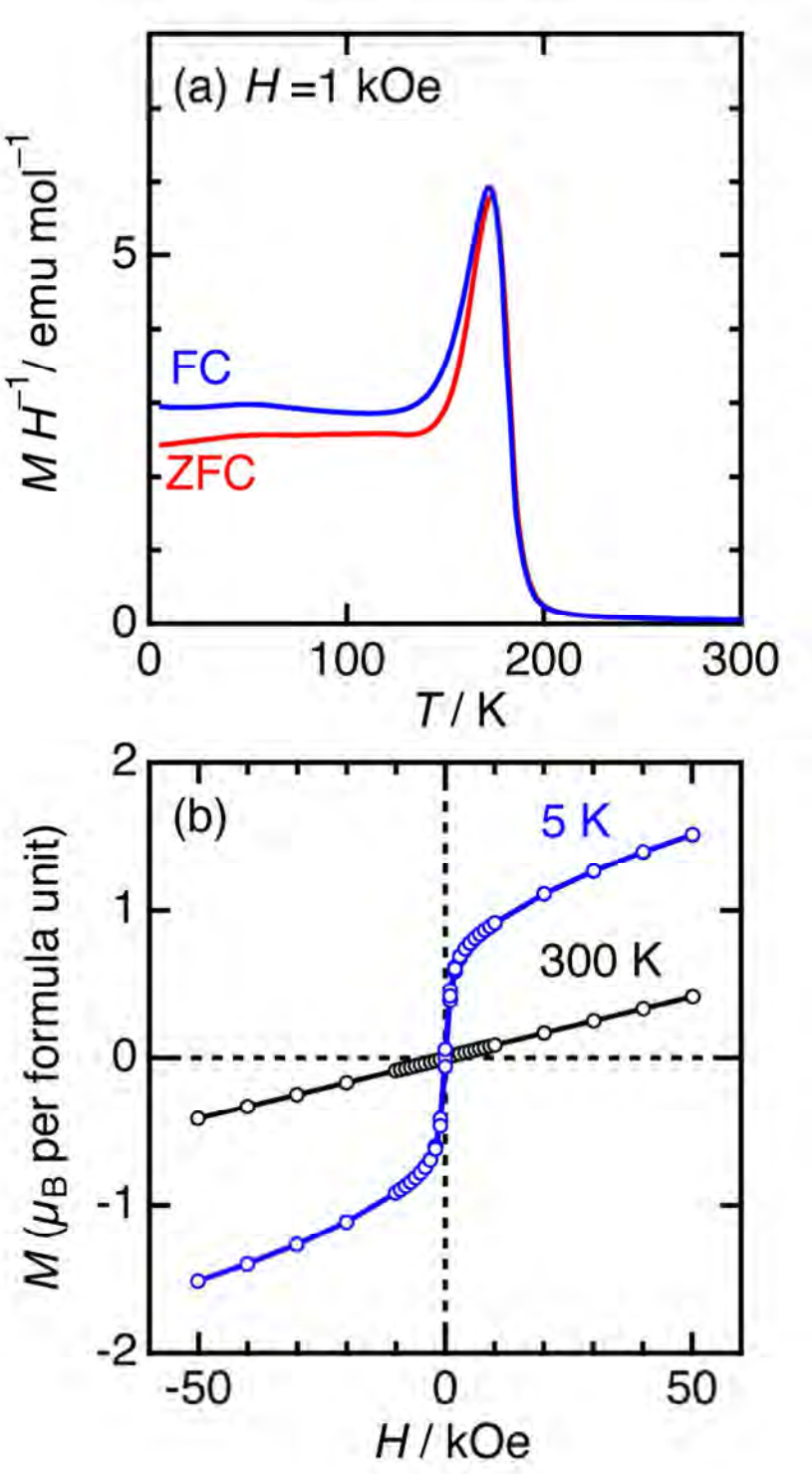
(a) H =1 kOe
M H⁻¹ / emu mol⁻¹
FC
ZFC
T / K
(b)
5 K
300 K
M (μB per formula unit)
H / kOe

Figure 5

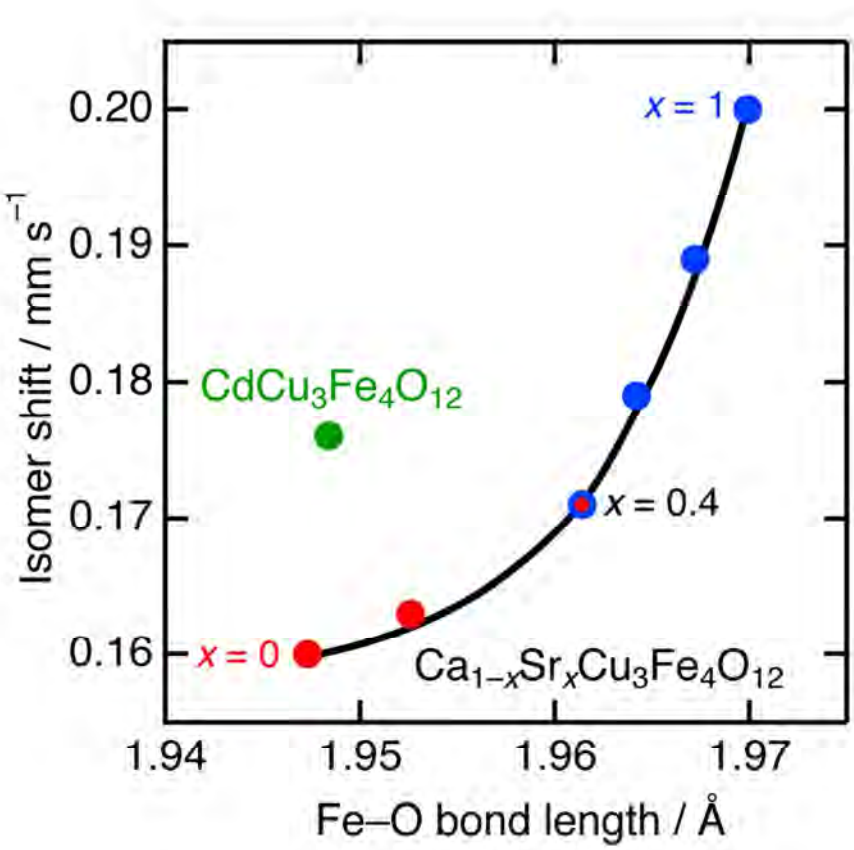
0.20
0.19
0.18
0.17
0.16
Isomer shift / mm s^{-1}
x = 1
$CdCu_3Fe_4O_{12}$
x = 0.4
x = 0
$Ca_{1-x}Sr_xCu_3Fe_4O_{12}$
1.94
1.95
1.96
1.97
Fe–O bond length / Å

Figure 6

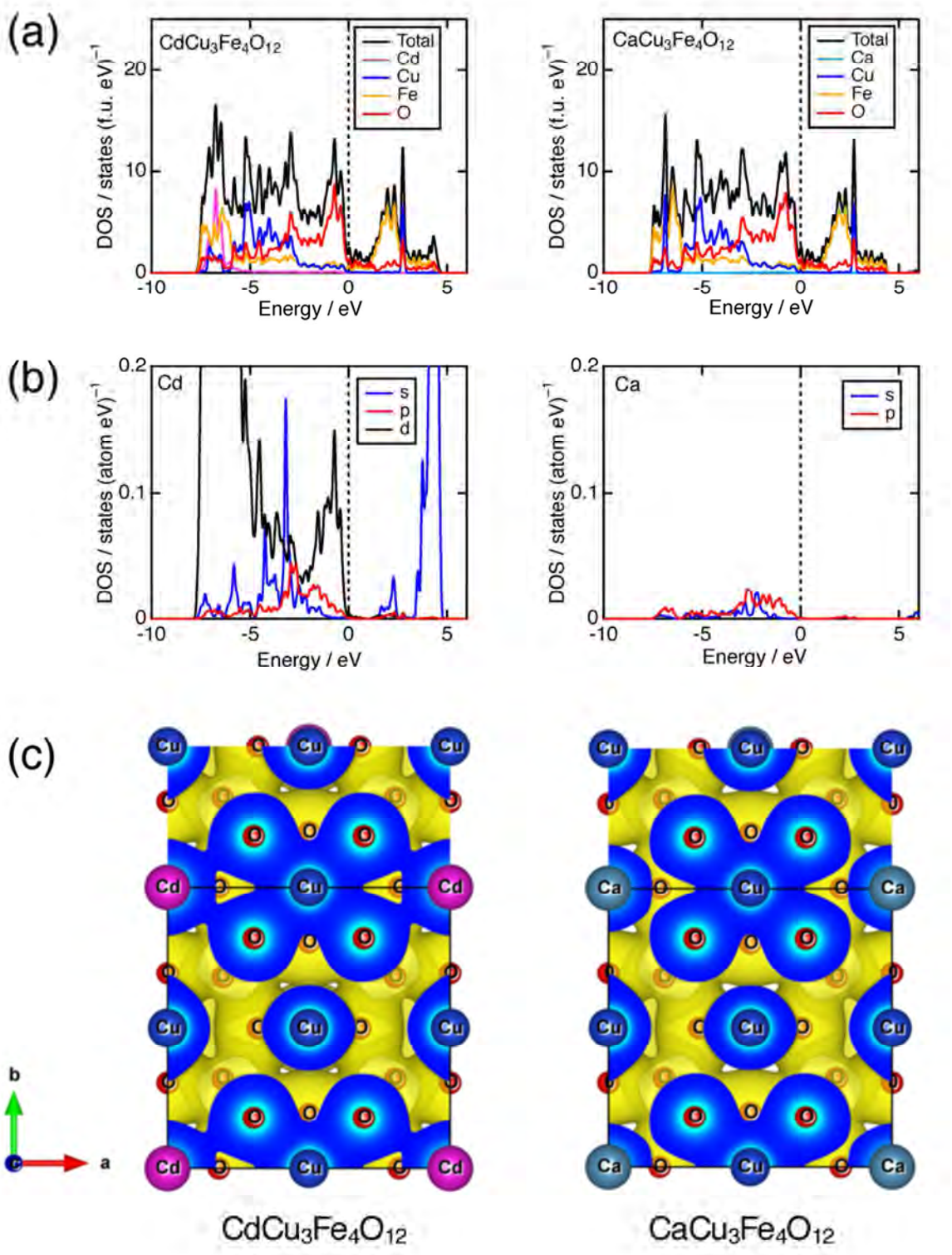
(a)
CdCu3Fe4O12
Total
Cd
Cu
Fe
O
DOS / states (f.u. eV)−1
Energy / eV
CaCu3Fe4O12
Total
Ca
Cu
Fe
O
(b)
Cd
s
p
d
DOS / states (atom eV)−1
Energy / eV
Ca
s
p
(c)
b
a
CdCu3Fe4O12
CaCu3Fe4O12

Figure 7

For Table of Contents Only

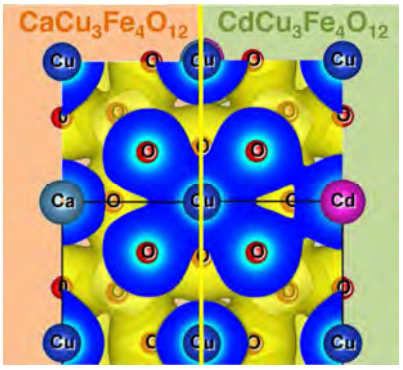

We demonstrate high-pressure synthesis, crystal structure, and properties of a new quadruple perovskite $CdCu_3Fe_4O_{12}$. $CdCu_3Fe_4O_{12}$ undergoes a charge disproportionation of Fe ions without charge ordering below ~200 K. First-principle calculations and Mössbauer spectroscopy display that covalent Cd–O bonds effectively suppress the Fe–O bond covalency, resulting in the electronic state different from that of the isoelectronic compound $CaCu_3Fe_4O_{12}$. This finding proposes covalency competition among constituent metal ions dominating electronic states of complex metal oxides.